

The Modified Ghost Fluid Method as Applied to Extreme Fluid-Structure Interaction in the Presence of Cavitation

T. G. Liu^{1,*}, B. C. Khoo² and W. F. Xie¹

¹ *Institute of High Performance Computing, #01-01 The Capricorn, Singapore Science Park II, Singapore 117528.*

² *Department of Mechanical Engineering, National University of Singapore, Singapore 119260.*

Received 30 September 2005; Accepted (in revised version) 13 March 2006

Abstract. In this work, the modified Ghost Fluid Method is further developed to apply to compressible fluid coupled to deformable structure, where the pressure in the structure or flow can vary from an initial extremely high magnitude (such that the solid medium can be under plastic compression) to a subsequently very low quantity (so that cavitation can occur in the fluid). New techniques are also developed in the definition of the ghost fluid status when the structure is under plastic deformation or when the flow is under cavitation next to the structure. Numerical results show that the improved MGFM for treatment of the fluid-deformable structure coupling works efficiently for all pressure ranges and is capable of simulating cavitation evolution and cavitation reloading in conjunction with the employment of the isentropic one-fluid cavitation model.

Key words: Ghost fluid method (GFM); modified ghost fluid method (MGFM); one-fluid cavitation model; cavitation reloading; cavitation-structure interaction.

1 Introduction

Cavitation occurs in fluid flow when the low pressure in the liquid reaches the limit of saturated vapour pressure. One example is the flow generated by an underwater explosion near a structure and a free surface, where (bulk) cavitation just below the free surface and (hull) cavitation nearby the structure are usually created and subsequently collapse very violently. As cavitation collapse can induce a strong pressure surge, the loading caused by

*Correspondence to: T. G. Liu, Institute of High Performance Computing, #01-01 The Capricorn, Singapore Science Park II, Singapore 117528. Email: liutg@ihpc.a-star.edu.sg

an underwater explosion on the nearby structure physically consists of direct underwater shock loading and cavitation reloading. Traditionally, the shock loading is considered as a major if not the sole contributor to the structural failure. With the advances of experimental and numerical techniques, some recent experiments and numerics have shown that cavitation can affect the pressure loading of the structure significantly [5, 21, 22, 43, 44]. Brett et al. [5] conducted a series of experiments investigating a cylinder deformation associated with underwater explosions. The cavitation reloading on the structure arising from the cavitation collapse can be clearly observed in their experimental results. The underwater experiments and numerical simulations carried out by Wardlaw and Luton [43] in a cylindrical container further showed that the peak pressure caused by cavitation collapse can be up to 40% of the peak pressure associated with the initial/direct shock impact. Recent numerical simulations by Liu et al. [21] and Xie et al. [44] also affirmed that the pressure surge caused by cavitation collapse near a rigid wall can attain up to 40%~50% of the said peak pressure. Consequently, it is important and perhaps critical to ascertain correctly the possible cavitation reloading on the structure in order to assess accurately the overall loading.

From the viewpoint of numerical simulation, however, it is still extremely challenging to fully simulate the flows generated by an underwater explosion near a deformable structure. There are several difficulties encountered in the modelling and simulating of such unsteady flows. These are summarised as follows

- 1) The structural deformation and compressibility have to be taken into account. Under the impact of a strong underwater shock, the solid structure can behave like a fluid and strong transmitted compression waves can propagate inside the structure.
- 2) Fluid phase transition or cavitation has to be modelled in order to capture the possible cavitation reloading on the structure.
- 3) The fluid-structure non-linear interaction has to be faithfully captured. This is perhaps the most difficult and challenging part in the numerical simulation. The said interaction is usually simplified as in previous numerical works, especially those calculated using commercial software.
- 4) The treatment of the moving explosive gas-water interface and the free surface is another key challenge.

Some recent analysis and discussions on the influence of a free surface on the structural loading may be found in [22]. The treatment of the moving gas-water interface and discussions on shock wave refraction at a moving gas-water interface can be found in [24, 25]. Discussions on various unsteady cavitation models may be found in [21].

In this work, the focus is on the treatment of the moving fluid-structure interface, which plays a key role in the accurate evaluation of the shock loading and cavitation reloading on the structure. On the other hand, it is well known that the treatment of moving material interfaces is still very challenging, especially if the density ratio of the two media is very large (like air-water flow) or one of the media is constituted with a

stiff equation of state (like the present solid medium); the difficulties are associated with the numerical oscillations generated in the vicinity of the material interface(s). Such oscillations (especially pressure oscillations) are partly analyzed mathematically by Karni [15]. To suppress the oscillations, various techniques have been developed [1, 2, 7, 14, 15, 19, 20, 38]. With these techniques, numerical oscillations can be greatly suppressed and even completely removed. On the other hand, such additional techniques inevitably made the integrated algorithms much more complex, computationally more costly and even the non-trivial extension to multi-dimensions. In order to overcome those mentioned difficulties, a flexible technique called ghost fluid method (GFM) was recently developed by Fedkiw et al. [9] to treat the moving material interface and simultaneously keep the simplicity of the Eulerian method. The key point of the GFM-based algorithm is to properly define the ghost fluids, which is the main difference among the various GFM-based algorithms [1, 3, 9, 11, 16, 24, 42]. The relatively easy extension to multi-dimensions is one of its main advantages. However, which GFM-based algorithm is most appropriate was found to be problem-related [23, 24]. To develop a more universally applicable GFM, Liu et al [24] proposed the modified Ghost Fluid Method (MGFM), where an approximate Riemann problem solver (ARPS) was employed to predict the ghost fluid status. The MGFM has been shown to be robust and efficient when applied to gas-gas or gas-liquid compressible flows [23, 24, 42].

In this work, our intent is to apply the MGFM to treat the fluid-deformable structure interface. Since a solid medium can be under plastic deformation due to the strong impact of a shock wave, resulting in a leading elastic wave and a trailing plastic wave propagating simultaneously in the solid medium. In such a situation, the influence of structural permanent deformation on the fluid-structure coupling has to be taken into account in the definition of the ghost fluid status. To do so, the ARPS will be further developed to take into account the influence of structure plastic deformation. The possible appearance of cavitation causes further difficulties in predicting and defining the ghost fluid states in the late stage of fluid-structure interaction. A new technique will also be developed to define the ghost fluid status in such situations based on the physical fact that the acoustic impedance of a solid medium is usually far larger than that of the cavitating flow and that the pressure inside the cavitation region is physically quite low. One will find that the improved MGFM technique for treating the fluid-structure coupling can ensure that the MGFM-based algorithm work effectively for all pressure ranges from the initial very high pressure (where the structure experiences elastic or even plastic compression) to the subsequent much lower pressure environment (where fluid flow cavitation can occur next to the interface). The present developed MGFM together with the isentropic one-fluid cavitation model developed recently in [21] is capable of capturing the shock loading as well as the cavitation reloading.

The remaining text is organized as follows. The Euler equations with the EOS for gases, water and solid structure are presented in Section 2 together with the isentropic one-fluid model for cavitating flow. In Section 3, the MGFM is briefly introduced and then new techniques will be developed to define the ghost fluid status for the situations

when the structure is under plastic deformation or the fluid is under cavitation next to the structure. In Section 4 various examples with analytical solutions available are used to validate the present method. The present method is then applied to multi-dimensional fluid-deformable structure coupling to capture the shock loading and cavitation reloading. A brief conclusion is given in Section 5.

2 Governing equations

One of the intents of the present work is to simulate the underwater explosion near a structure so as to evaluate the shock loading as well as the cavitation reloading. In the simulation, explosive gas flow, compressible water flow with possible cavitation and compressible solid medium are involved. The Euler equations for 2D compressible explosive gas, compressible water and fluid-like solid medium can be written in a consistent form as

$$\frac{\partial U}{\partial t} + \frac{\partial F(U)}{\partial x} + \frac{\partial G(U)}{\partial y} = S(U), \tag{2.1}$$

$$p = p(e, \rho). \tag{2.2}$$

The respective expressions of U , F , G and S for explosive gas flow are given as

$$U = \begin{bmatrix} \rho \\ \rho u \\ \rho v \\ \rho E \end{bmatrix}, \quad F = \begin{bmatrix} \rho u \\ \rho u^2 + p \\ \rho uv \\ (E + p)u \end{bmatrix}, \quad G = \begin{bmatrix} \rho v \\ \rho uv \\ \rho v^2 + p \\ (E + p)v \end{bmatrix}, \quad S = -\frac{(n-1)}{r} \begin{bmatrix} \rho u \\ \rho u^2 \\ \rho uv \\ (E + p)u \end{bmatrix}. \tag{2.3}$$

Here, ρ is the gas flow density, p is the pressure, u and v are the flow velocity components in the respective x and y directions. E is the total energy and given as $E = \rho e + 0.5\rho(u^2 + v^2)$, where e is the internal energy per unit mass. n is a system parameter which takes on a value of 1 or 2. If n is set equal to 1, system (2.1) is for planar 2D flow; if n is set equal to 2, it is for 2D axis-symmetric flow. As water, solid and cavitating flow are assumed compressible and barotropic, the total energy equation is not required to be solved directly and thus not employed in the computation.

For cavitating flow, we employ the one-fluid model to simulate the cavitation evolution. The flow (averaged) density is then expressed as

$$\rho = \alpha\rho_g + (1 - \alpha)\rho_l.$$

Here, ρ_l is the density of water component, ρ_g is the density of vapor component and α is the void fraction. If α is set to 0, it becomes a pure liquid (water) flow, while if α is set to 1, the flow is a pure gas (vapour).

The level set technique [29] is employed to capture the locations of the explosive gas-water and water-structure interfaces. The governing equation to advance the level set

function $\phi(x, y)$ can be expressed as

$$\frac{\partial \phi}{\partial t} + u \frac{\partial \phi}{\partial x} + v \frac{\partial \phi}{\partial y} = 0. \quad (2.4)$$

The level set function is usually the signed distance function with re-initialisation in order to maintain the accuracy [35]. In the present study, equation (2.4) is numerically solved via the second-order method developed in [20].

Equation (2.2) is taken as the equation of state (EOS) for closure of system (2.1). The γ -law is assumed valid for gases and can be written as

$$\rho e = \frac{p}{\gamma_g - 1} \quad (2.5)$$

where γ_g is the ratio of specific heats for the gas. Physically, the JWL equation is a more accurate EOS for explosive gases. On the other hand, the simple perfect gas law is also frequently employed to constitute the explosive gases but with γ_g usually not less than 2. In this work, the perfect gas law is used and γ_g is set to be 2.0 for the explosive gases only for computational purpose. The application of the JWL EOS using GFM or MGFM-based algorithms can be found in [9, 24], respectively.

Tait's EOS is used for compressible water and given as

$$p = B \left(\frac{\rho}{\rho_{10}} \right)^N - B + A. \quad (2.6)$$

Here, B and A are constants and set equal to $3.31 \times 10^8 Pa$ and $10^5 Pa$, respectively, while $\rho_{10} = 1000 kg/m^3$ is the reference density for water, and N is set to be 7.15. It may be noted that there are several versions of EOS for water. Among them, Tait's equation is the simplest. We should emphasize that the techniques to be developed in this work can be easily applied to a more general EOS.

The Tait EOS can also be employed to constitute the solid medium [26]. Using Tait's EOS, however, makes no distinction between the material under plastic and elastic deformation; there is only one wave generated in the structure even under plastic deformation. Physically, there are both elastic and plastic waves propagating in the structure under plastic deformation. The more accurate EOS for compressible solid medium is the Hydro-Elasto-Plastic EOS [37], which is expressed as

$$p = \begin{cases} p_h(\rho) + \frac{2}{3}Y, & \rho \geq \rho_2 \\ p_h(\rho) + \frac{4}{3}(G \ln(\rho/\rho_0) + \tau_0), & \rho_1 < \rho \leq \rho_2 \\ p_h(\rho) - \frac{2}{3}Y, & \rho < \rho_1, \end{cases} \quad (2.7a)$$

with

$$p_h(\rho) = \frac{m}{\beta} \left((\rho/\rho_a)^\beta - 1 \right) + p_a. \quad (2.7b)$$

Here, m , Y , G and β are the bulk modulus, the yield stress, the modulus of rigidity and a model constant, respectively. The subscript “0” refers to an initial state. ρ_a is the solid density at pressure (stress) p_a , which is usually taken to be one atmosphere. $\rho_1 = \rho_0 e^{-(2\tau_0+Y)/2G}$ and $\rho_2 = \rho_0 e^{-(2\tau_0-Y)/2G}$. We note that the associated stresses at ρ_1 and ρ_2 as p_1 (negative) and p_2 (positive), respectively. Once the solid stress is beyond p_2 , the solid is under plastic compression, while if the stress (negative) in the solid is below p_1 the solid is under plastic tension. There are two waves generated when the solid is under plastic deformation. One is a leading elastic wave and the other is a trailing plastic wave. More details on EOS (2.7a) can be found in [37].

In the modeling of transient cavitating flow, there are generally two different approaches. One is called the two-fluid method [17, 30, 32]. The other is the one-fluid method [8, 18, 40, 41]. The first approach assumes that both phases co-exist and each phase is governed by its own set of differential equations. Because the exchange of mass, momentum and energy is treated explicitly as transfer terms in this approach and the parameters relating to phase exchange are generally unknown, the two-fluid model is seldom employed to the unsteady cavitation flow of the present interest.

On the contrary, the one-fluid method treats the cavitating flow as a mixture of two fluids behaving as one. Thus, one set of differential equations expresses the whole fluid motion. The one-fluid model is relatively easy to treat the dynamic creation and collapse of cavitation. Since the cavitation dimension and pressure surge caused by cavitation collapse are the major concerns in the underwater explosion, the developed methods for modelling such unsteady cavitation flows are usually one-fluid methods and governed by the Euler equations, where the flow viscosity, thermal conductivity, surface tension and turbulence are generally neglected.

The application of a one-fluid cavitation model can be implemented as follows

$$p = \begin{cases} \text{Tait's EOS,} & \text{if } p \geq p_{sat} \\ \text{Cavitation Model,} & \text{if } p < p_{sat} \end{cases}, \quad (2.8)$$

where p_{sat} is the physical saturated pressure. The commonly used one-fluid cavitation models in underwater explosions are the Cut-off model [43] and the Vacuum model [36]. Both are essentially pure-fluid models without phase exchange taken into account. Schmidt et al. [31] developed a one-fluid model for modeling high-speed cavitating nozzles. However, the Schmidt model can only work effectively for small size cavitation with a small ratio of vapor density to surrounding liquid density (less than 10^{-5}) as shown in [21, 44].

Recently Liu et al. [21] successfully developed a mathematically consistent and physically reasonable one-fluid cavitation model called isentropic one-fluid cavitation model via assuming that the cavitating flow is a homogenous mixture consisting of isentropic vapour and water components. If the cavitating mixture is assumed homogenous, one can rigorously obtain the governing equation for the evolution of void fraction

$$\frac{d\alpha}{dp} = \alpha(1 - \alpha) \left(\frac{1}{\rho_l a_l^2} - \frac{1}{\rho_g a_g^2} \right), \quad (2.9)$$

which further leads to the equation of state for the mixture,

$$\frac{\alpha}{1 - \alpha} = k \frac{(\bar{p}/\bar{p}_{cav})^{1/N}}{(p/p_{cav})^{1/\gamma}}, \quad (2.10)$$

$$\rho = \frac{k\rho_g^{cav} + \rho_l^{cav}}{(\bar{p}/\bar{p}_{cav})^{-1/N} + k(p/p_{cav})^{-1/\gamma}}, \quad (2.11)$$

where $k = \alpha_0/(1 - \alpha_0)$. ρ_g^{cav} and ρ_l^{cav} are the associated gas and water density at the cavitation pressure $p_{cav} \leq p_{sat}$, respectively. α_0 is the known void fraction of the mixture density at p_{sat} . Thus, the EOS for the water with the isentropic one-fluid cavitation model can be written as

$$\rho = \begin{cases} \rho_{l0} \left(\frac{p + B - A}{B} \right)^{1/N} & p \geq p_{sat}, \\ \frac{k\rho_g^{cav} + \rho_l^{cav}}{(\bar{p}/\bar{p}_{cav})^{-1/N} + k(p/p_{cav})^{-1/\gamma}} & p < p_{sat}. \end{cases} \quad (2.12)$$

The void fraction is calculated using (2.10) once the pressure is obtained via (2.11) using iteration. The isentropic one-fluid cavitation model has several good features in comparison to the other existing one-fluid models. It will be employed in the present study and simulations of cavitating flow. Detailed analysis and discussion about this model and other previous cavitation models may be found in [21].

3 The MGFm applied to fluid-structure coupling

3.1 The GFM-based algorithm

In a GFM-based algorithm, the level set technique is usually employed to capture the moving interface. With the employment of ghost cells and the definition of ghost fluids, the GFM makes the interface “invisible” during the computation of flow field such that its extension to multi-dimensions becomes fairly simple. The GFM-based algorithm holds some very good properties in contrast to previous conservative methods. These are:

- 1) There are no difficulties in constructing the numerical flux in the vicinity of the interface; construction of an efficient and correct numerical flux over a fixed mesh for many existing conservative method is usually very involved and computationally expensive (even more so in multi-dimension) [7, 20].
- 2) There is no ambiguity in the use of EOS in the updating of the solution; which EOS should be employed in the updating of the solution for the mixture cells can be less clear for a traditional conservative method. As a consequence, an artificial EOS is usually introduced for overcoming this difficulty [2, 14, 34, 38].
- 3) A sharp interface is maintained; the smearing of the material interface leads to low accuracy in the vicinity of the interface and usually triggers numerical oscillations for a more traditional conservative method [1, 15].

- 4) A GFM-based algorithm is easily extended to multi-dimensions; the additional techniques used to suppress and remove the numerical oscillations usually lead to a non-trivial extension of the method to multi-dimensions for several existing conservative methods [20, 38].
- 5) Each medium can be solved using one's own favourite solver [6]; this is a unique property of a GFM-based method.
- 6) Each medium can have very different properties (and to some extent EOS) from another [6]; that is one medium can be compressible and/or inviscid and another be incompressible and/or viscous.

The GFM-based algorithms have been successfully applied to various areas such as the treatment of discontinuities in compressible and incompressible flows [6, 33], flame and detonation fronts [10, 28], and fluid-structure coupling [26, 45]. On the other hand, a GFM-based algorithm is usually non-conservative. There are attempts to make the GFM-based algorithm conservative [4, 12, 27]. However, an efficient and practical conservative GFM-based algorithm has yet to be developed. The other issue for the GFM-based algorithm is that its performance depends on the definition of the ghost fluid status and the implicit capture and imposition of boundary conditions at the moving interface. In fact, in order for a Ghost Fluid Method (GFM)-based algorithm to work correctly, Conditions [23] must be satisfied and the influence of wave interaction at the material interface and the effect of material properties on the interfacial status have to be faithfully taken into account in the definition of the ghost fluid status [23, 24, 42].

3.2 The modified ghost fluid method (MGFM)

The modified GFM (MGFM) [24] has been shown to be very robust. In the MGFM, the ghost fluid states are defined using the interfacial states, which are obtained via solving a defined multi-medium Riemann problem along the normal direction of the interface using the two non-linear characteristic equations intersecting at the material interface. There are two nonlinear characteristics intersecting at the interface; one stems from the left medium flow while the other originates from the right medium flow. They can be written in association with system (2.1) along the normal direction of the interface as

$$\frac{dp_{I+}}{dt} + \rho_{IL}c_{IL}\frac{du_{nI+}}{dt} = S_{I+}, \quad \text{along} \quad \frac{dr_{nI+}}{dt} = u_{nI} + c_{IL}, \quad (3.1a)$$

$$\frac{dp_{I-}}{dt} - \rho_{IR}c_{IR}\frac{du_{nI-}}{dt} = S_{I-}, \quad \text{along} \quad \frac{dr_{nI-}}{dt} = u_{nI} - c_{IR}, \quad (3.1b)$$

where subscripts “*I*”, “*IL*”, “*IR*” refer to the interface, the left side of the interface and the right side of the interface, respectively. The subscripts “+” and “-” indicate that the derivatives are evaluated and approached from the left and right sides of the interface, respectively. $\rho_{IL}(\rho_{IR})$ and $c_{IL}(c_{IR})$ are the density and sound speed on the left (right) side of the interface; S_{I+} and S_{I-} are the remaining terms associated with system (2.1), which are explicitly treated; u_{nI} and p_I are the normal velocity and pressure at the interface.

$r_n = \vec{r} \cdot \vec{n}$, $u_n = \vec{V} \cdot \vec{n}$ and $\vec{n} = \nabla\phi/|\nabla\phi|$, where \vec{r} is the position vector and ϕ is the level set function. We solve system (3.1) to obtain the interfacial status and then use this predicted interfacial status to define the ghost fluid status in the MGFm.

System (3.1) has to be specially solved to ensure the correct shock wave refraction at the interface. As such, an approximate Riemann problem solver (ARPS) based on a doubled shock structure is employed [20] to solve system (3.1) and can then be written as

$$\frac{p_I - p_{IL}}{W_l} + (u_{nI} - u_{nIL}) = \Delta t S_{I+}, \quad (3.2a)$$

$$\frac{p_I - p_{IR}}{W_r} - (u_{nI} - u_{nIR}) = \Delta t S_{I-}, \quad (3.2b)$$

$$W_l = \sqrt{\frac{p_I - p_{IL}}{1/\rho_{IL} - 1/\rho_L(p_I)}}, \quad W_r = \sqrt{\frac{p_I - p_{IR}}{1/\rho_{IR} - 1/\rho_R(p_I)}}. \quad (3.2c)$$

Here, $\rho_L(p_I)$ and $\rho_R(p_I)$ are the shocked fluid densities at pressure p_I for the left and right shock waves, respectively. The left shock wave has a flow pressure p_{IL} and velocity $u_{IL} + \Delta t S_{I+}$ ahead of the shock front, while the right shock wave possesses a flow pressure p_{IR} and velocity $u_{IR} - \Delta t S_{I-}$ ahead of the shock front. Here Δt is the time step size. Using (3.2a) and (3.2b), an implicit function of p_I is obtained and has to be solved iteratively for p_I . In order to get the interfacial status via system (3.1), the flow states U_{nIL} and U_{nIR} on the respective left and right sides of the interface along the two non-linear characteristic lines in the normal direction have to be obtained in advance. U_{nIL} and U_{nIR} are usually obtained via interpolation in the respective left and right media.

3.3 Defining ghost fluid status under structure plastic deformation

We assume that the fluid is located on the left side of the interface, while the structure is on the right side of the interface. The ARPS (3.2) can then be expressed as

$$\frac{p_I - p_{IL}}{W_l} + (u_{nI} - u_{nIL}) = \Delta t S_{I+}, \quad (3.3a)$$

$$\frac{p_I - p_{IR}}{W_r} - (u_{nI} - u_{nIR}) = \Delta t S_{I-}, \quad (3.3b)$$

$$W_l = \sqrt{\frac{p_I - p_{IL}}{1/\rho_{IL} - 1/\rho_w(p_I)}}, \quad W_r = \sqrt{\frac{p_I - p_{IR}}{1/\rho_{IR} - 1/\rho_s(p_I)}}, \quad (3.3c)$$

using EOS (2.6) for water and EOS (2.7a) for the solid medium. Here $\rho_w(p_I)$ and $\rho_s(p_I)$ are the respective water and solid densities at pressure p_I .

The success of the ARPS (3.2) as applied to the gas-gas or gas-water Riemann problem depends on that there is at most one non-linear Riemann wave admitted in each medium to connect the interface, and that the said non-linear wave must connect with the initial status. If the solid is under elastic deformation, the solution structure of a fluid-solid Riemann problem with EOS (2.7a) is similar to that of a gas-gas or gas-water Riemann

problem, system (3.3) thus can be directly employed to predict the interfacial status in such situations. On the other hand, there can be two non-linear Riemann waves in the solid medium when the solid medium is under plastic deformation. In such a situation, the history of solid deformation must be known and recorded in order to obtain the solid state. In other words, the influence of both plastic and elastic waves has to be taken into account in order to accurately determine the interfacial status. Since the non-linear Riemann wave next to the interface in the solid medium actually connects to the state behind the elastic wave when the solid medium is under plastic deformation, the influence of the elastic wave has to be taken into account first and then the plastic wave in order to correctly determine the interfacial status in solving system (3.1). To do so, U_{nIR} must be replaced by U_2 —the state behind the elastic wave. This leads to the following ARPS used when the solid is under plastic deformation:

$$\frac{p_I - p_{IL}}{W_l} + (u_{nI} - u_{nIL}) = \Delta t S_{I+}, \quad (3.4a)$$

$$\frac{p_I - p_2}{W_r} - (u_{nI} - u_{nIR2}) = \Delta t S_{I-}, \quad (3.4b)$$

$$W_l = \sqrt{\frac{p_I - p_{IL}}{1/\rho_{IL} - 1/\rho_w(p_I)}}, \quad W_r = \sqrt{\frac{p_I - p_2}{1/\rho_2 - 1/\rho_s(p_I)}}. \quad (3.4c)$$

Here, $u_{nIR2} = u_{nIR} + \sqrt{(p_2 - p_{IR})(1/\rho_{IR} - 1/\rho_2)}$, which is obtained via the shock relationship for the leading elastic shock wave with U_{nIR} as the state ahead of the shock front. System (3.4) will be employed to predict the interfacial status when the interfacial pressure is beyond p_2 such that the solid medium is under plastic deformation.

3.4 Defining ghost fluid status under low pressure and fluid cavitation

The ARPS (3.3) works efficiently if the pressure ratio of fluid to the structure is high. On the other hand, because iteration is required in solving (3.3), the convergence is not efficient when the pressure inside the solid is not very high due to the extreme insensitivity of density change in response to the pressure change. (In such situations, the structure is under elastic deformation). To increase the computational efficiency, the ARPS (3.3) was replaced by an explicit characteristic method in such situations [26]. This technique also works well for the Hydro-Elasto-Plastic EOS. More specifically, the acoustic impedances of $\rho_{IL}c_{IL}$ and $\rho_{IR}c_{IR}$ are assumed constant, resulting in the direct solution of (3.3) as

$$\frac{p_I - p_{IL}}{\rho_{IL}c_{IL}} + (u_{nI} - u_{nIL}) = \Delta t S_{I+}, \quad (3.5a)$$

$$\frac{p_I - p_{IR}}{\rho_{IR}c_{IR}} - (u_{nI} - u_{nIR}) = \Delta t S_{I-}. \quad (3.5b)$$

Theoretical analysis has shown [26] that system (3.5) indeed provides accurate interfacial status if the pressure ratio is not high (less than $10E4$). Numerical results to be given in

Section 4 will show that the non-iterative system (3.5) works indeed far efficiently than the iterative system (3.3) in the low-pressure situations (see Cases 1 & 2 in Section 4).

Cavitation frequently occurs due to fluid-structure interaction. Once cavitation appears next to the structure, tension waves (negative stress) may exist next to the interface in the structure. As a result, a negative p_{IR} may be erroneously obtained, leading to a negative interfacial pressure calculated using (3.3) or (3.5). The interfacial pressure, however, should never be negative physically due to the presence of flow cavitation. This leads to the inapplicability of both (3.3) and (3.5). Special treatment to the interface in such situations, thus, has to be introduced. Because the pressure in the cavitation region is below the saturated vapor pressure, which is very low (can be very close to zero), the pressure change across the interface is small. Furthermore, due to the physical fact that a solid medium is relatively extremely incompressible, the acoustic impedance ($\rho_{IR}c_{IR}$) of solid is very large with a magnitude usually and typically above $\mathcal{O}(10E6)$ kgm/s. As a result, the magnitude of $dp_{I-}/(\rho_{IR}c_{IR})$ becomes negligibly small (usually less than $1.0E-5$ m/s). Consequently, system (3.1) can reasonably be reduced to

$$\frac{dp_{I+}}{dt} + \rho_{IL}c_{IL} \frac{du_{nI+}}{dt} = S_{I+}, \quad \text{along} \quad \frac{dr_{nI+}}{dt} = u_{nI} + c_{IL}, \quad (3.6a)$$

$$du_{nI-} = \frac{dtS_{I-}}{\rho_{IR}c_{IR}}, \quad \text{along} \quad \frac{dr_{nI-}}{dt} = u_{nI} - c_{IR}. \quad (3.6b)$$

Because the structural stress is not involved in (3.6b), the involvement of negative p_{IR} in predicting the interfacial status is avoided when tension waves appear next to the interface in the structure. A simple yet efficient way to numerically solve (3.6) is to assume $\rho_{IL}c_{IL}$ as locally constant. As such, system (3.6) can be solved to directly obtain the interface pressure and velocity as follows:

$$p_I = p_{IL} + \rho_{IL}c_{IL} \left[u_{nIL} - u_{nIR} - \frac{\Delta t S_{I-}}{\rho_{IR}c_{IR}} \right] + \Delta t S_{I+}, \quad (3.7a)$$

$$u_I = u_{nIR} + \frac{\Delta t S_{I-}}{\rho_{IR}c_{IR}}. \quad (3.7b)$$

System (3.7) does not always guarantee a positive pressure unless $u_{nIL} - u_{nIR}$ is a positive value or at most a negative value of small magnitude [26]. In the problems of present interest, this condition is satisfied as the cavitation occurs in the late stage, where the fluid-structure interface is well balanced. In fact, numerical results have showed that $u_{nIL} - u_{nIR}$ is always a small positive value in the present computation. For the cavitating flow initiated by a sudden pull or motion of the solid boundary, in which $u_{nIL} - u_{nIR}$ is expected to be a negative value of large quantity, system (3.7) may fail to provide a positive interfacial pressure. How to define the ghost fluid state in such a situation is still an open question and subject of further research.

Here we summarize the procedure of predicting the interfacial status for various pressure situations.

1. Identify the interfacial cell and obtain the interfacial location, which is defined by the level set function $\phi(x, y) = 0$
2. Calculate the interfacial normal direction via $\vec{n} = \nabla\phi/|\nabla\phi|$
3. Obtain U_{IL} and U_{IR} via interpolation along the respective characteristic lines, and project U_{IL} and U_{IR} in the normal direction to obtain U_{nIL} and U_{nIR} .
4. Predict the interfacial pressure and normal velocity via iteratively solving (3.3) if the pressure ratio of p_{IL}/p_{IR} is high (larger than 1.0E4), or via directly solving (3.5) if the pressure ratio of p_{IL}/p_{IR} is not very high (less than 1.0E4) and both p_{IL} and p_{IR} are larger than the water saturated pressure p_{sat} , or via formula (3.7) if either p_{IL} or p_{IR} is less than the water saturated pressure p_{sat} ; if the calculated interfacial pressure is high than p_2 , use system (3.4) to recalculate the interfacial status.
5. Calculate the interfacial densities on the left and right sides via the respective EOS employed. More specifically, if the predicted p_I is less than p_{sat} , the EOS (2.12) is used to obtain the interfacial density for the cavitating flow side in conjunction with the Tait EOS; the EOS for the solid medium is applied to calculate the structural density at the interface.
6. Calculate the x - and y - velocity components on both sides of the interface comprising the interfacial normal velocity component obtained in Step 4 and the interfacial tangential velocity component, which can be easily obtained via interpolation.

3.5 The integrated MGF algorithm

Once the interfacial states are obtained, the ghost fluid status can be easily defined by following the similar procedure as outlined in [24, 42]. Here we outline the procedure of defining the ghost fluid status using the MGF algorithm for two dimensions. We assume the computational domain is rectangular. First, we define a rectangular computational sub-domain $[I_{1K}, I_{2K}] \times [J_{1K}, J_{2K}]$ and an identification matrix S_K for each medium (the k^{th} medium), where $S_K(i, j) = 1$ if the grid point (i, j) is taken by the k^{th} medium, otherwise it is set to 0. We carry out the computation for each medium respectively, and denote the result by U_K^{n+1} after evaluating the ghost points within its computational domain. Then the final solution in the new time step is given by $U^{n+1} = \sum S_K^{n+1} U_K^{n+1}$ where S_K^{n+1} is the new identification matrix of the k^{th} medium, which is obtained in advance by the level set technique. One can define a computational domain for each medium that includes boundary points and grid points in the interfacial regions associated with this medium within a band of 2 to 4 grid points defined by $|\phi| < \varepsilon$. Here ϕ is the level set distance function and ε is set to be about $3 \min(\Delta x, \Delta y)$; Δx and Δy are spatial step sizes in the respective x and y directions. Within the band of $|\phi| < \varepsilon$, if a grid point, say $(i0, j0)$, is identified to be next to the interface, one then follows the procedure described in Section 3.4 to obtain the interfacial status. This predicted interfacial status is then used to define the flow status at the point $(i0, j0)$. Once all the ghost fluid points next to the interface have been defined, one then iteratively solves the following convective equation (3.8) to steady state to propagate the predicted interfacial status to other ghost

fluid points in the band; the fluid status at the real fluid points and the ghost fluid points next to the interface is fixed during the iteration of (3.8) given as

$$\frac{\partial q}{\partial t} \pm \vec{n} \cdot \nabla q = 0. \quad (3.8)$$

Here $q = [\rho, u, v, p]^T$ and $\vec{n} = \nabla\phi/|\nabla\phi|$. If the normal direction of the level set function (i.e. the normal direction of the interface) points towards the ghost fluid side, the plus sign “+” is taken, otherwise the minus sign “-” is taken. To impose the continuity of pressure and the normal velocity at the interface and therefore further reduce the conservative errors in the integrated MGF algorithm, the real fluid status just next to the interface may also be replaced using the predicted interfacial status as used in [42]. This technique is applied to Cases 1 & 2 in Section 4.

4 Applications

Various gas-gas, gas-water, gas-solid and water-solid problems have previously been applied to test the MGF algorithm [23, 24, 42]. In this section, applications are focused on fluid-structure coupling; the resultant pressure in the fluid side varies from extremely high to very low value. The present integrated MGF algorithm will also be employed to capture the cavitation evolution and cavitation reloading during an underwater explosion near a compressible structure. All computations are carried out using the MUSCL scheme [39] with the HLL approximate Riemann solver [13]. All parameters are non-dimensionalized unless otherwise noted. γ_g is set to 2.0 for explosive gas, N and non-dimensional B are set to be 7.15 and 3.31E3 for water, respectively. The solid structure is assumed to be steel in this work. β , non-dimensional m , non-dimensional Y and non-dimensional G , the parameters associated with EOS (2.7a) are set to be 3.7, 6.0135E5, 9.79E3 and 8.53E5, respectively. The non-dimensional τ_0 , p_a and ρ_a are set to be 0.0, 1.0 and 7.8, respectively. B , m , G , Y and pressure are non-dimensionalized with respect to 1.0E5Pa, the density is non-dimensionalized via 1000kg/m³ and velocity is non-dimensionalized via 10m/s. We emphasize again that taking into account the wave interaction and the influence of material properties in the definition of the ghost fluid status is crucial for a GFM-based algorithm to provide the correct solutions for the problems studied here.

Case 1: This is a 1D water-solid Riemann problem with the solid under low-pressure compression. The initial conditions for water on the left are $u_l = 0.0$, $p_l = 10.0$ and $\rho_l = 1.0$, while the initial conditions for the solid (steel) are $u_r = 0.0$, $p_r = 1.0$ and $\rho_r = 7.8$. The computational domain is $[0, 1]$ with total 401 grid points uniformly distributed. The interface is initially located at 0.4 and CFL is set to 0.7. We run the computation to 6.66E-4. Figs. 1(a), 1(b) and 1(c) show the respective velocity profiles computed via (3.5), (3.3) with iteration convergence up to 10E-6 and (3.3) with iteration convergence up to 10E-15 to predict the interfacial status. The analytical solution is provided for comparison. From these Figures, it is clearly shown that (3.5) works quite efficiently in this given low

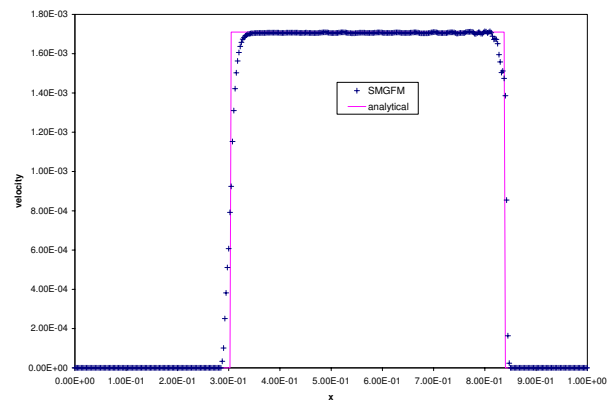
pressure situation, while using (3.3), double-precision computation with sufficiently high iteration convergence must be applied in order to ensure the MGF algorithm provides comparable results with that using (3.5). This demonstrates that using the simplified system (3.5) to predict the interfacial status is indeed a better choice than using system (3.3) in the low-pressure situation in terms of both computational efficiency and accuracy.

Case 2: This is also a 1D water-solid Riemann problem with the solid under not very high-pressure compression. The initial conditions for water on the left are $u_l = 0.0$, $p_l = 100.0$ and $\rho_l = 1.005$, while the initial conditions for the solid are $u_r = 0.0$, $p_r = 1.0$ and $\rho_r = 7.8$. The computational domain is $[0, 1]$ with total 401 uniform grid points used. The interface is initially located at 0.4 and CFL is set to 0.9. Figs. 2(a), 2(b) and 2(c) show the respective velocity profiles at $t=8.56E-4$ computed via (3.5), (3.3) with iteration convergence condition of $10E-6$ and (3.3) with iteration convergence condition of $10E-12$ to predict the interfacial status with comparison to the analytical solution. Similarly, the MGF algorithm of using (3.5) to predict the interfacial status works computationally more efficiently than that using (3.3). In fact, numerical tests showed that (3.5) can work very well to provide correct interfacial status if the pressure ratio is less than $1.0E4$.

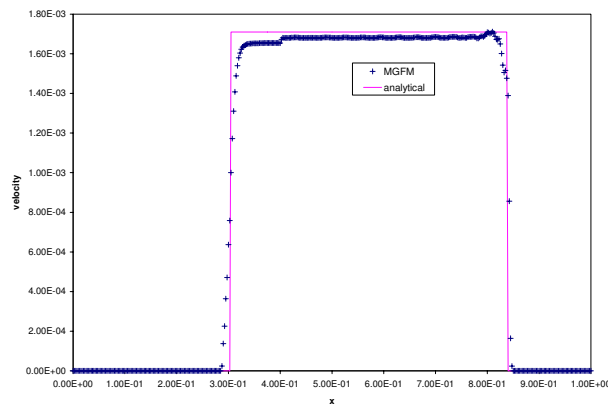
Case 3: This is a problem of highly-pressurized water next to a steel wall, where the steel is still in elastic deformation. The initial conditions for water on the left are $u_l = 0.0$, $p_l = 10000.0$ and $\rho_l = 1.23$, while the initial conditions for the steel are $u_r = 0.0$, $p_r = 1.0$ and $\rho_r = 7.8$. (3.3) is employed to predict the ghost fluid status. The computational domain is $[0, 1]$ with total 201 uniform grid points. The interface is initially located at 0.4 and CFL is set to 0.9. Figs. 3(a) and (b) show the numerical velocity and pressure profiles in comparison to the analytical solution at $t=6.82E-4$. The agreement between the numerical results and the analytical is reasonable.

Case 4: This is a problem of extremely high pressure in water such that the solid is under plastic deformation. The initial conditions for water on the left are $u_l = 0.0$, $p_l = 80000.0$ and $\rho_l = 1.607$, while the initial conditions for the solid are $u_r = 0.0$, $p_r = 1.0$ and $\rho_r = 7.8$. (3.4) is employed to predict the ghost fluid status. The computational domain is $[0, 1]$ and there are in total 201 uniform grid points used. The interface is initially located at 0.4 and CFL is set to 0.9. Figs 4(a) and (b) show the numerical velocity and pressure profiles in comparison to the analytical solution at $t=6.79E-4$. Both the elastic shock wave and the plastic shock wave in the structure are captured correctly. The agreement between the numerical results and the analytical is reasonable.

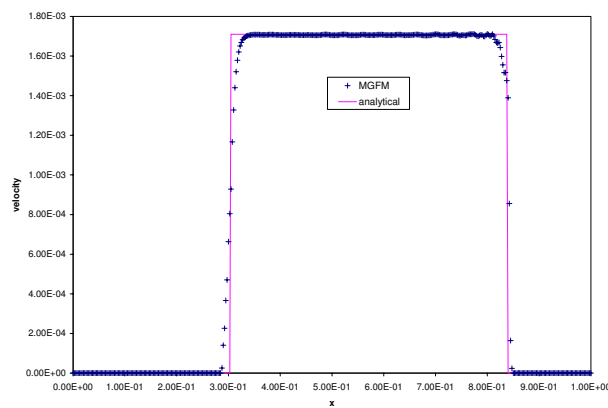
Case 5: This is a highly pressurized water stream impacting on the structure such that the structure is under plastic compression. The initial conditions for water stream are $u_l = 50.0$ and $p_l = 50000.0$. The structure is initially assumed to be stationary. The computational domain is $[0, 1]$ with 201 uniform grid points used. The interface is initially located at 0.5 and CFL is set to 0.9. Figs. 5(a) and (b) show the numerical results compared to the exact solution well at $t=6.79E-4$. Both the elastic shock wave and the plastic shock wave are captured correctly by the present integrated MGF.



(a)

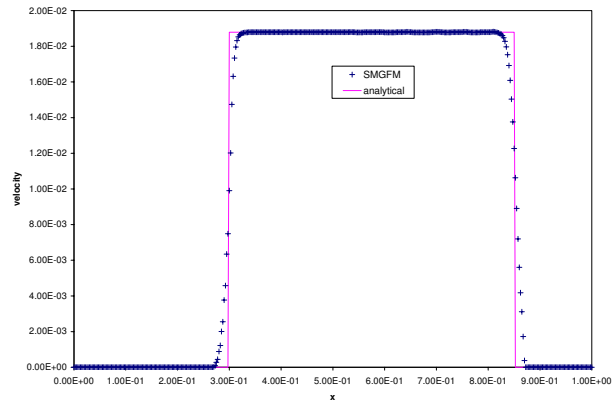


(b)

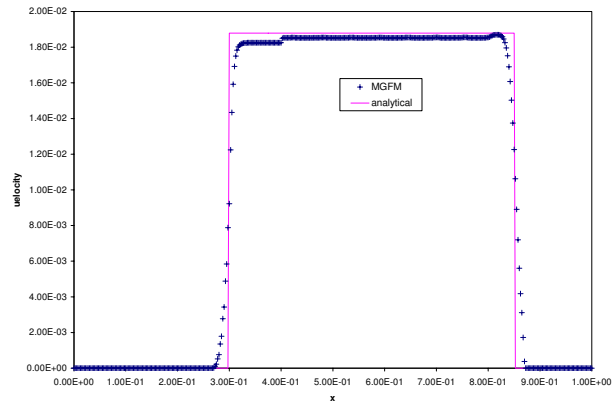


(c)

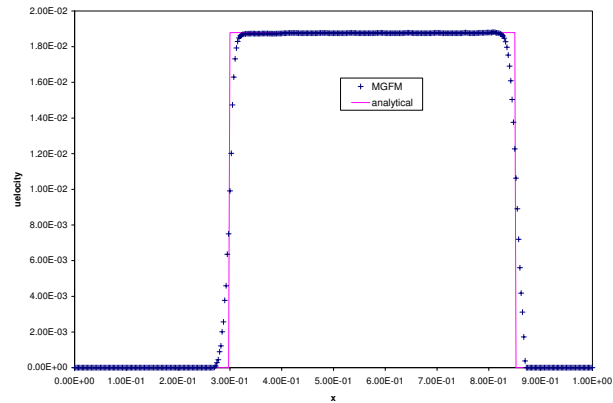
Figure 1: (a) The velocity profile obtained using (3.5) for Case 1 at $t=6.66E-4$. (b) The velocity profile obtained using (3.3) with convergence $10E-6$ for Case 1 at $t=6.66E-4$. (c) The velocity profile obtained using (3.3) with high convergence $10E-15$ for Case 1 at $t=6.66E-4$.



(a)



(b)



(c)

Figure 2: (a) The velocity profile obtained using (3.5) for Case 2 at $t=8.56E-4$. (b) The velocity profile obtained using (3.3) with convergence $10E-6$ for Case 2 at $t=8.56E-4$. (c) The velocity profile obtained using (3.3) with high convergence $10E-12$ for Case 2 at $t=8.56E-4$.

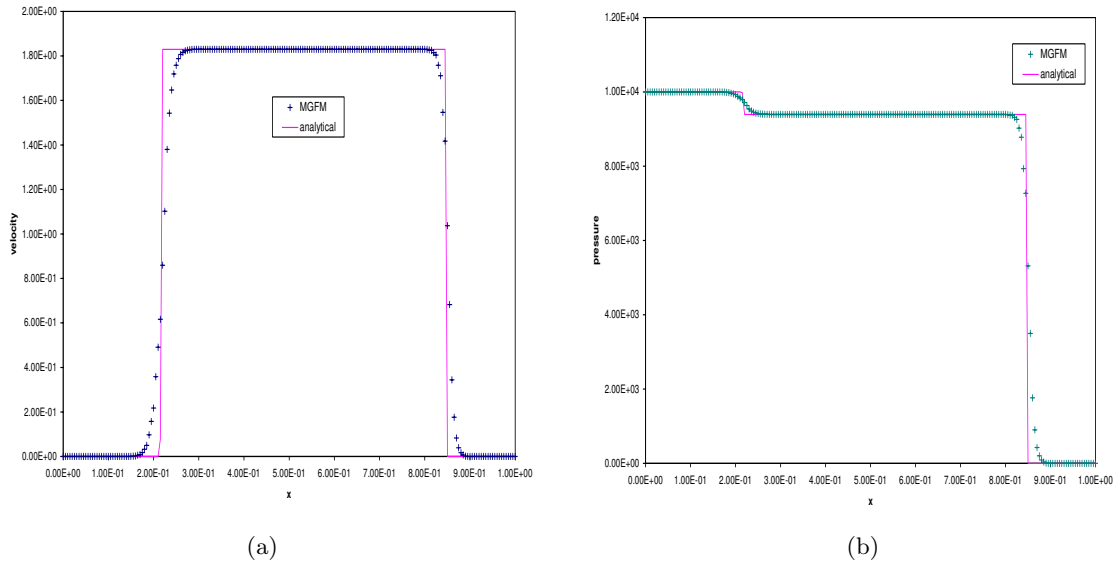


Figure 3: (a) The velocity profile obtained using (3.3) for Case 3 at $t=6.82E-4$. (b) The pressure profile obtained using (3.3) for Case 3 at $t=6.82E-4$.

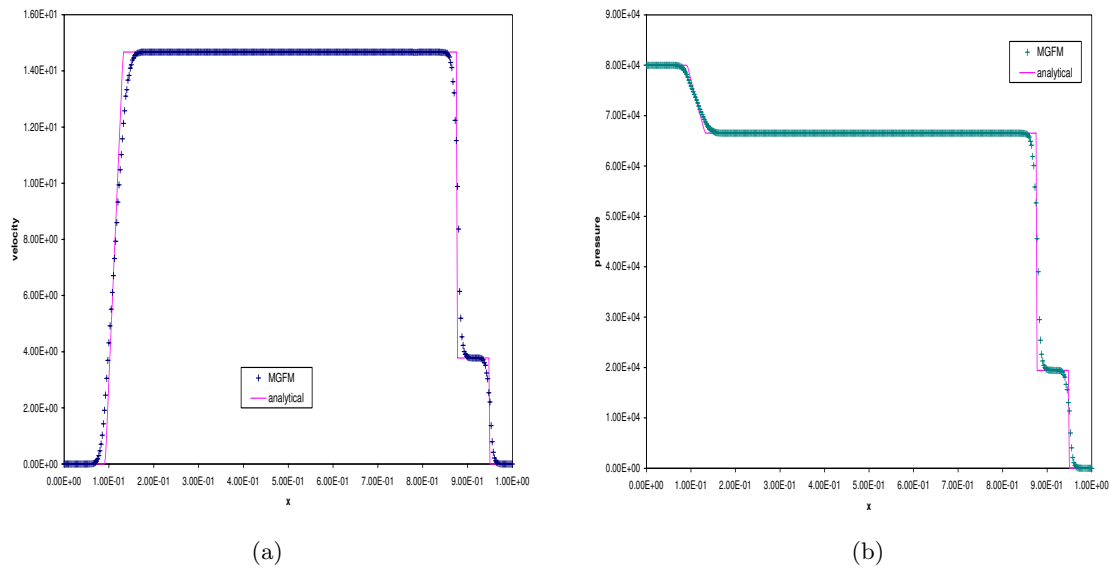


Figure 4: (a) The velocity profile obtained using (3.4) for Case 4 at $t=6.79E-4$. (b) The pressure profile obtained using (3.4) for Case 4 at $t=6.79E-4$.

Case 6: This is a case of an underwater explosion near a planar structure. A high pressure air cylinder of unit radius is located at the origin (0.0,0.0) in water and the initial flow parameters inside the explosive bubble are $\rho_g=1270.0\text{kg/m}^3$, $p_g=8290\text{bar}$,

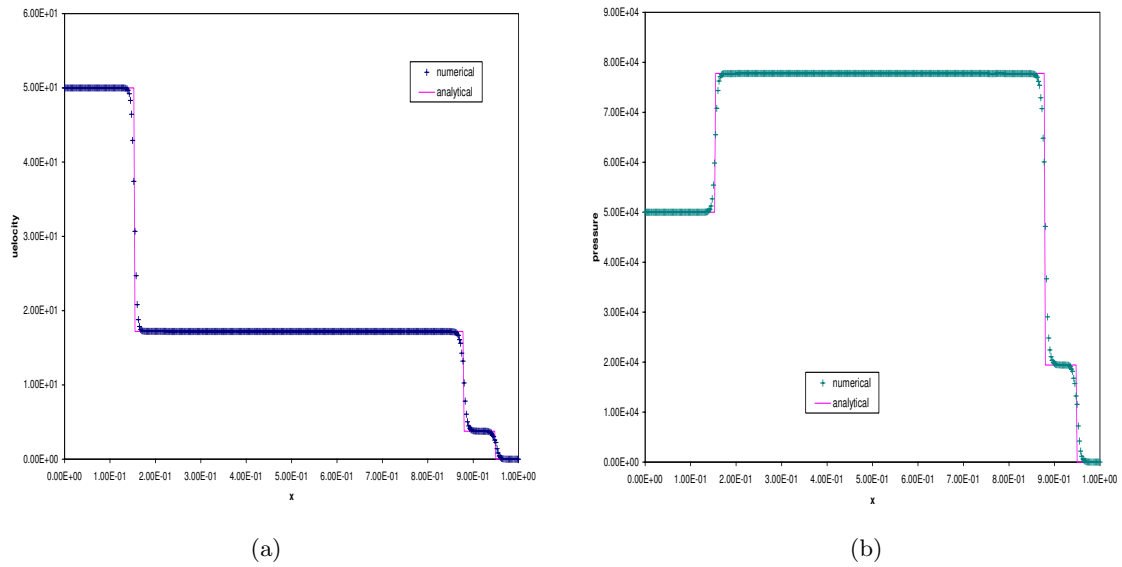


Figure 5: (a) The velocity profile obtained using (3.4) for Case 5 at $t=6.79E-4$. (b) The pressure profile obtained using (3.4) for Case 5 at $t=6.79E-4$.

$u_g=0.0\text{m/s}$ and $v_g=0.0\text{m/s}$. The initial flow parameters for water are $\rho_w=1000.0\text{kg/m}^3$, $p_w=1.0\text{bar}$, $u_w=0.0\text{m/s}$ and $v_w=0.0\text{m/s}$. The initial conditions for the (compressible) solid are $\rho_s=7800.0\text{kg/m}^3$, $p_s=1.0\text{bar}$, $u_s=0.0\text{m/s}$ and $v_s=0.0\text{m/s}$. The computational domain is set to be $[-6, 6] \times [-6, 6]$ and the planer wall is located at the straight line $y = 3.361 \times 361$ uniform grid points are distributed. CFL is taken to be 0.45. This is a challenging problem. In the earlier stage, the pressure is very high such that the structure compression has to be taken into account, while the subsequently pressure becomes very much lower near the structure such that flow cavitation occurs in the later stage. p_{sat} is set to be 0.05bar. The integrated GFM algorithm also works well for this problem.

Once the explosion starts, a strong underwater shock is generated and propagates radially outwards with decreasing strength. The underwater (incident) shock soon impacts the structure (wall), resulting in the incident shock partly reflected from the structure surface and partly transmitted into the structure. Due to the large sound speed of the structure, the transmitted shock wave inside the structure travels faster than the incident underwater shock, leading to the formation of a precursive wave propagating on the structure surface, which soon travels outside the computational domain. The reflection wave with a decreasing strength travels towards the expanding explosion bubble surface (see Fig. 6(a)). As a result of shock-bubble interaction, a rarefaction wave forms [25] and propagates towards the structure. The interaction of the rarefaction wave and the deformation of structure causes a low pressure region to be formed next to the structure. As time goes on, the pressure there keeps on decreasing such that the pressure in the low pressure region drops below p_{sat} , leading to the incipience of cavitation and flow phase transition (see Fig. 6(b)).

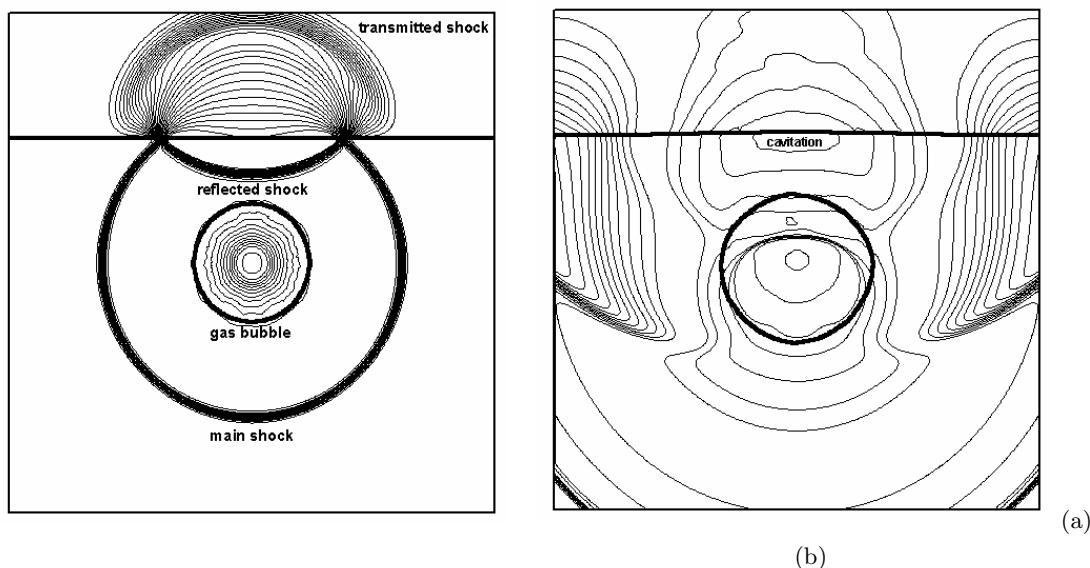


Figure 6: (a) Pressure contour for Case 6 at $t=1.5\text{ms}$. (b) Pressure contour for Case 6 at $t=4.0\text{ms}$.

Because the surrounding flow pressure is higher than that inside the cavitation region, the water flows back and causes the cavitation collapse. The cavitation collapse generates a pressure surge, which imposes cavitation reloading on the structure. After the cavitation collapse, the cavitating flow becomes pure liquid again. To better observe the process of cavitation creation and collapse and the effect of structure flexibility on the cavitation collapse, the pressure history at the centre of planar wall is recorded for two types of wall: rigid and compressible walls (see Fig. 7). In Fig. 7, the recorded first pressure peak is due to the direct underwater shock impact, while the second pressure peak is due to cavitation collapse. It is found that the structure flexibility affects the shock impact significantly and causes the cavitation collapse to occur earlier.

5 Conclusions and future work

The long-time simulation of fluid-structure nonlinear coupling/interaction over a wide pressure ranges is still very challenging because of the appearance of fluid phase transition (cavitation), the fluidization of solid under extreme compression and the extreme incompressibility of solid under low pressure. In this work, employment of the modified Ghost Fluid Method (MGFM) for treating the fluid-structure interface have been presented where it has been further developed to be applicable to compressible fluid coupled to deformable structure in all pressure ranges. To define the ghost fluid states when the structure is under plastic deformation, an approximate Riemann problem solver (ARPS), which is able to take into account the structure plastic deformation, has been developed. To handle and simulate cavitation structure interaction, the non-linear characteristics intersecting at

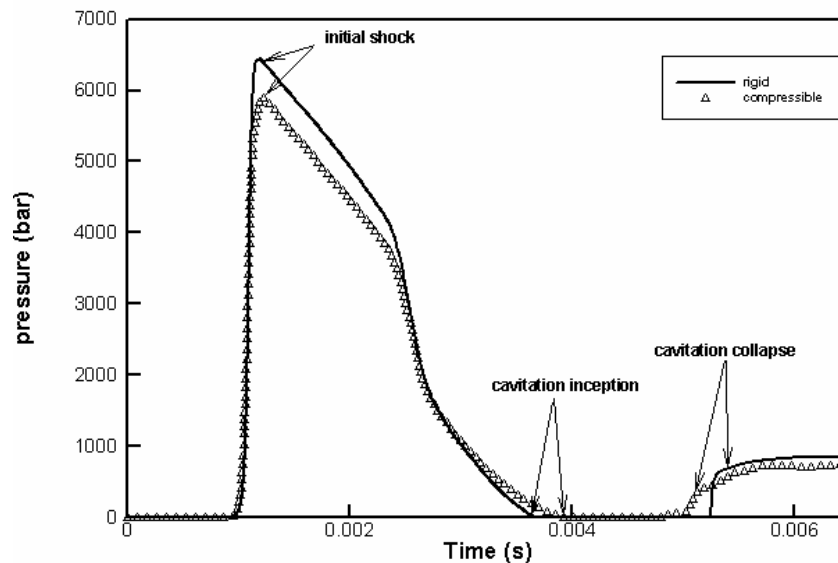


Figure 7: The pressure histories for Case 6 at the center location of the planar wall.

the material interface has been employed and specially solved in order to obtain a physically reasonable interface state and thus defining the ghost fluid states in such situations. The accuracy and efficiency of the developed MGFm in this work have been verified and applied to various challenging problems including the case of shock loading and cavitation reloading during an underwater explosion. Numerical results showed that the present (integrated) MGFm indeed works efficiently under all pressure environments.

The present developed technique of treating the fluid-structure coupling will be applied in future work to simulate supercavitating flow over a high-speed deformable body (where there is cavitation inception, development and collapse), underwater explosion below a free surface (where bulk cavitation occurs) and shock-cavitation-structure interaction in biological flows (as in shock lithotripsy treatment for the removal of kidney stones). The extension of the MGFm to treat the fluid-elastic material coupling is also underway, where wide industrial and other biological applications are expected. Besides the numerical study on associated flow dynamics, theoretical analysis on issues related to accuracy of the different existing GFM algorithms are works planned in the pipeline.

References

- [1] R. Abgrall and S. Karni, Computations of compressible multifluids, *J. Comput. Phys.*, 169 (2001), 594-623.
- [2] R. Abgrall, How to prevent pressure oscillations in multicomponent flow calculations: A quasi-conservative approach, *J. Comput. Phys.*, 125 (1996), 150-160.

- [3] T. D. Aslam, A level set algorithm for tracking discontinuities in hyperbolic conservation laws II: Systems of equations, *J. Sci. Comput.*, 19 (2003), 37-62.
- [4] D. A. Bailey, P. K. Sweby and P. Glaister, A ghost fluid, moving finite volume plus continuous remap method for compressible Euler flow, *Int. J. Numer. Meth. Fl.*, 47 (2005), 833-840.
- [5] J. M. Brett, G. Yiannakopoulos and P. J. van der Schaaf, Time-resolved measurement of the deformation of the submerged cylinders subjected to loading from a nearby explosion, *Int. J. Impact Eng.*, 24 (2000), 875-890.
- [6] R. Caiden, R. P. Fedkiw and C. Anderson, A numerical method for two-phase flow consisting of separate compressible and incompressible regions, *J. Comput. Phys.*, 166 (2001), 1-27.
- [7] J.-P. Cocchi and R. Saurel, A Riemann problem based method for the resolution of compressible multimaterial flows, *J. Comput. Phys.*, 137 (1997), 265-298.
- [8] Y. Delannoy and J. L. Kueny, Two phase flow approach in unsteady cavitation modelling, in: *Cavitation and Multiphase Flow Forum, FED-98*, pp. 152-158, 1990.
- [9] R. P. Fedkiw, A. Marquina and B. Merriman, A non oscillatory eulerian approach to interfaces in multimaterial flows (The ghost fluid method), *J. Comput. Phys.*, 152 (1999), 457-492.
- [10] R. P. Fedkiw, T. Aslam and S. Xu, The ghost fluid method for deflagration and detonation discontinuities, *J. Comput. Phys.*, 154 (1999), 393-427.
- [11] R. P. Fedkiw, Coupling an Eulerian fluid calculation to a Lagrangian solid calculation with the ghost fluid method, *J. Comput. Phys.*, 175 (2002), 200-224.
- [12] J. Glimm, L. Xia, Y. Liu and N. Zhao, Conservative front tracking and level set algorithms, *PNAS*, 98 (2001), 14198-14201.
- [13] A. Harten, P. D. Lax and B. van Leer, Upstream differencing and Godunov-type schemes for hyperbolic conservation laws, *SIAM Rev.*, 25 (1983), 35-61.
- [14] P. Jenny, B. Muller and H. Thomann, Correction of conservative Euler solvers for gas mixtures, *J. Comput. Phys.*, 132 (1997), 91-107.
- [15] S. Karni, Multi-component flow calculations by a consistent primitive algorithm, *J. Comput. Phys.*, 112 (1994), 31-43.
- [16] B. Koren, M. R. Lewis, E. H. van Brummelen and B. van Leer, Riemann-problem and level-set approaches for homentropic two-fluid flow computations, *J. Comput. Phys.*, 181 (2000), 654-674.
- [17] A. Kubota, H. Kato and H. Yamaguchi, A new modelling of cavitating flows: A numerical study of unsteady cavitation on a hydrofoil section, *J. Fluid Mech.*, 240 (1992), 59-96.
- [18] R. F. Kunz, D. A. Boger, D. R. Stinebring, T. S. Chyczewski, J. W. Lindau, H. J. Gibeling, S. Venkateswaran and T. R. Govindan, A preconditioned Navier-Stokes method for two-phase flows with application to cavitation prediction, *Comput. Fluids*, 29 (2000), 849-875.
- [19] S. Jiang and G. Ni, A γ -model BGK scheme for compressible multifluids, *Int. J. Numer. Meth. Fl.*, 46 (2004), 163-183.
- [20] T. G. Liu, B. C. Khoo and K. S. Yeo, The simulation of compressible multi-medium flow. Part I: A new methodology with applications to 1D gas-gas and gas-water cases, *Comput. Fluids*, 30 (2001), 291-314.
- [21] T. G. Liu, B. C. Khoo and W. F. Xie, Isentropic one-fluid modelling of unsteady cavitating flow, *J. Comput. Phys.*, 201 (2004), 80-108.
- [22] T. G. Liu, B. C. Khoo, K. S. Yeo and C. Wang, Underwater shock-free surface-structure interaction, *Int. J. Numer. Meth. Eng.*, 58 (2003), 609-630.
- [23] T. G. Liu, B. C. Khoo and C. W. Wang, The ghost fluid method for compressible gas-water simulation, *J. Comput. Phys.*, 204 (2005), 193-221.
- [24] T. G. Liu, B. C. Khoo and K. S. Yeo, Ghost Fluid Method for strong shock impacting on

- material interface, *J. Comput. Phys.*, 190 (2003), 651-681.
- [25] T. G. Liu, B. C. Khoo and K. S. Yeo, The simulation of compressible multi-medium flow. Part II: Applications to 2D underwater shock refraction, *Comput. Fluids*, 30 (2001), 315-337.
 - [26] T. G. Liu, W. F. Xie and B. C. Khoo, The modified ghost fluid method for compressible fluid coupled to compressible structure, submitted.
 - [27] D. Q. Nguyen, F. Gibou and R. Fedkiw, A fully conservative ghost fluid method & stiff detonation waves, in: *The 12th International Detonation Symposium*, San Diego, CA. 2002.
 - [28] D. Q. Nguyen, R. P. Fedkiw and M. Kang, A boundary condition capturing method for incompressible flame discontinuities, *J. Comput. Phys.*, 172 (2001), 71-98.
 - [29] S. Osher and A. Sethian, Fronts propagating with curvature-dependent speed: Algorithms based on Hamilton-Jacobi formulation, *J. Comput. Phys.*, 79 (1988), 12-49.
 - [30] R. Saurel and O. Lemetayer, A multiphase model for compressible flows with interfaces, shocks, detonation waves and cavitation, *J. Fluid Mech.*, 431 (2001), 239-271.
 - [31] D. P. Schmidt, C. J. Rutland and M. L. Corradini, A fully compressible, two-dimensional model of small, high speed, cavitating nozzles, *Atomization Spray.*, 9 (1999), 255-276.
 - [32] I. Senocak and W. Shyy, A pressure-based method for turbulent cavitating flow computations, *J. Comput. Phys.*, 176 (2002), 363-383.
 - [33] S. Shin, Internal wave computations using the ghost fluid method on unstructured grids, *Int. J. Numer. Meth. Fl.*, 47 (2005), 233-251.
 - [34] K. M. Shyue, An efficient shock-capturing algorithm for compressible multicomponent problem, *J. Comput. Phys.*, 142 (1998) 208-242.
 - [35] M. Sussman, P. Smereka and S. Osher, A level set approach for computing solutions to incompressible two-phase flow, *J. Comput. Phys.*, 114 (1994), 146-159.
 - [36] H. S. Tang and D. Huang, A second-order accurate capturing scheme for 1D inviscid flows of gas and water with vacuum zones, *J. Comput. Phys.*, 128 (1996), 301-318.
 - [37] H. S. Tang and F. Sotiropoulos, A second-order Godunov method for wave problems in coupled solid-water-gas systems, *J. Comput. Phys.*, 151 (1999), 790-815.
 - [38] E. H. van Brummelen and B. Kolen, A pressure-invariant conservative Godunov-type method for barotropic two-fluid flows, *J. Comput. Phys.*, 185 (2003) 289-308.
 - [39] B. van Leer, Towards the ultimate conservative difference schemes III: Upstream centred finite-difference schemes for ideal compressible flow, *J. Comput. Phys.*, 23 (1977), 263-275.
 - [40] S. Venkateswaran, J. W. Lindau, R. F. Kunz and C. L. Merkle, Computation of multiphase mixture flows with compressible effects, *J. Comput. Phys.*, 180 (2002), 54-77.
 - [41] Y. Ventikos and G. Tzabiras, A numerical method for the simulation of steady and unsteady cavitating flows, *Comput. Fluids*, 29 (2000), 63-88.
 - [42] C. W. Wang, T. G. Liu and B. C. Khoo, A real-ghost fluid method for the simulation of multi-medium compressible flow, *SIAM. J. Sci. Comput.*, 28 (2006), 278-302.
 - [43] A. B. Wardlaw and J. A. Luton, Fluid-structure interaction mechanisms for close-in explosions, *Shock Vib.*, 7 (2000), 265-275.
 - [44] W. F. Xie, T. G. Liu and B. C. Khoo, Application of a one-fluid model for large scale homogeneous unsteady cavitation: The modified Schmidt model, *Comput. Fluids.*, 2005, in press.
 - [45] K. Yokoi, F. Xiao, H. Liu and K. Fukasaku, Three dimensional numerical simulation of flows with complex geometries in a regular Cartesian grid and its application to blood flow in cerebral artery with multiple aneurysms, *J. Comput. Phys.*, 202 (2005), 1-19.